

# Towards a global map of the artificial all-sky brightness

M. Kocifaj,<sup>1\*</sup> S. Bará,<sup>2</sup> F. Falchi<sup>3,4</sup>

<sup>1</sup>*ICA, Slovak Academy of Sciences, Dúbravská cesta 9, 845 03 Bratislava, Slovakia*

<sup>2</sup>*A. Astronómica "Ío", 15005 A Coruña, Galicia*

<sup>3</sup>*Istituto di Scienza e Tecnologia dell'Inquinamento Luminoso (ISTIL), 36016 Thiene, Italy*

<sup>4</sup>*Departamento de Física Aplicada, Universidade de Santiago de Compostela, 15782 Santiago de Compostela, Galicia, Spain*

Accepted XXX. Received YYY; in original form ZZZ

## ABSTRACT

Modeling the hemispherical night sky brightness of anthropogenic origin is a demanding computational challenge, due to the intensive calculations required to produce all-sky maps with fine angular resolution including high-order scattering effects. We present in this Letter a physically consistent, semi-analytic two-parameter model of the all-sky radiance produced by an artificial light source that encodes efficiently the spectral radiance in all directions of the sky above the observer. The two parameters of this function are derived from the state of the atmosphere, the distance to the observer, and the source's angular and spectral emission pattern. The anthropogenic all-sky radiance at any place on Earth can be easily calculated by adding up the contributions of the surrounding artificial sources, using the information available from nighttime satellite imagery and ground-truth lighting inventories. This opens the way for the elaboration of a global world map of the artificial all-sky brightness.

**Key words:** light pollution – methods: statistical – methods: data analysis

## 1 INTRODUCTION

The knowledge of the hemispherical night sky brightness produced by the ever-growing expansion of outdoor lighting systems is a necessary step for characterizing the nighttime environment and monitoring the evolution of the night sky quality at present and potential astronomy observatory sites. Whereas several networks worldwide routinely gather data on the zenith night sky brightness in different photometric bands, comprehensive information on the all-sky distributions of the artificial radiance at nighttime is considerably more scarce. Excepting for a few observatories, the existing data sets are limited to the images acquired in specific observational campaigns, and the ones captured by the all-sky cameras existing in astronomic facilities for general purposes that not often include the quantitative measurement of the night sky radiance.

In this context, modelling the artificial night sky radiance is a reasonable option. Modelling is also an instrumental tool for astronomical and environmental impact assessment of new lighting projects and territorial planning of outdoor lighting systems. The required equations are derived from radiative transfer theory and have been largely optimised for this particular field in the last two decades. Canonical examples of their outcomes are the iconic First World

Atlas of the artificial night sky brightness (Cinzano et al. 2001) and its updated and enhanced version Falchi et al. (2016). These atlases display the brightness of the zenith sky in the Johnson-Cousins V band, for a world grid with a ground pixel resolution of 30 arcmin.

Modelling the all-sky, hemispherical radiance distribution produced by artificial lights is however a more demanding challenge. Generating a fine angular resolution sky map requires computing the artificial brightness in a large number of directions on the sky. This is a computationally expensive task, especially if narrow band spectral resolution is required and higher orders of scattering are to be included. One way of reducing the dimensionality of the problem is expressing the hemispheric radiance as a linear combination of suitable basis functions or modes as, e.g. Zernike or Legendre polynomials (Bará et al. 2015a,b). This approach allows to compress the information of a  $10^6$  pixel map into  $10^2$  modal coefficients, enabling a significant reduction of computational load. However, these polynomial bases were not specifically designed for describing the typical patterns of the artificial night sky, and hence are not expected to be the optimal ones for this task.

In this work we develop a two-parameter model that efficiently matches the spectral radiance in all directions of the sky above the observer calculated by means of accurate numerical procedures. This model allows for an additional reduction of two orders of magnitude in the num-

\* E-mail: kocifaj@savba.sk

ber of required parameters, in comparison with previous attempts based on polynomial bases. The model is physically grounded, not merely heuristic, and its two parameters are related by means of analytic expressions or look-up tables to the state of the atmosphere, the distance to the observer, and the source's angular and spectral emission pattern. The analytic expression for the sky radiance is formally coincident with the one described in [Kocifaj and Bará \(2019\)](#); however, the two parameters  $t$  and  $g$  are now generalized to encompass higher-order scattering effects (up to the 5th order), and are provided ab initio, as a part of the model, not estimated a posteriori from images captured on site.

## 2 THE MODEL

Unlike empirical approaches, we model the all-sky radiance as a function of two parameters,  $g$  and  $t$  which are commonly used to characterize the atmospheric environment ([Kocifaj and Bará 2019](#)). In radiative transfer theories  $g$  has relation to the mean asymmetry parameter of a turbid atmosphere, while the physics interpretation of  $t$  is possible via mean optical attenuation along the beam path from a light source to a measuring site. For a cloudless optically thin atmosphere  $g$  is derived from aerosol ( $P_a$ ) and Rayleigh ( $P_R$ ) scattering phase functions using aerosol ( $k_a$ ) and Rayleigh ( $k_R$ ) volume extinction coefficients as weighting factors (see e.g. Eq. 5 in ([Katkovsky et al. 2018](#)))

$$P(g, \theta) = \frac{P_a(g_a, \theta)\omega_a k_a + P_R(\theta)k_R}{k_a + k_R}. \quad (1)$$

Here  $\omega_a$  is the aerosol single scattering albedo and  $\theta$  is the scattering angle – i.e. angle contained by the directions of incident and scattered waves. Alike in the Earth's atmosphere, the above approach is also applied to various complex discrete media, including particles dispersed in e.g. seawater (e.g. Eq. 78 in [Fokou et al. \(2021\)](#)). The formula 1 has a solid theoretical foundation in studying light scattering processes at a low scale, involving small atmospheric volumes. However, multiple scattering of light along with non-uniform beam attenuation at inclined trajectories introduce multifaceted distortions to NSB patterns which are difficult to describe using Eq. 1. Therefore, the total scattering phase function,  $P(g, \theta)$ , in a clear atmosphere (for  $k_a = 0$ ) is highly unlikely to mimic that of  $P_R(\theta)$ . Although  $P_R(\theta)$  shows ideal symmetry for forward and backward hemispheres with the peak ratio  $P_R(0^\circ)/P_R(90^\circ)=2$ , the radiance in multiply scattering Rayleigh atmosphere spans a wider range, resulting in  $P_R(0^\circ)/P_R(90^\circ)>2$  (see also leftmost plot in Fig. 12 in [Mobley \(2015\)](#) for sky elements at a horizontal circle; i.e. for zenith angle  $z$  being fixed). Assuming that  $z$  is conserved, the changes to the sky radiance  $L(z, A)$  are driven only by the scattering angle  $\theta$ , as it follows from the model by [Kocifaj and Bará \(2019\)](#)

$$L(z, A) = L_S P(g, \theta) \frac{(1-g)^2}{(1+g)} \frac{M(z)}{M_S t} \frac{e^{[M_S - M(z)]t} - 1}{M_S - M(z)} \quad (2)$$

Looking at the horizon, the above formula reduces to  $L_S P(g, \theta) \frac{(1-g)^2}{(1+g)}$ . In Eq. 2  $z$  and  $A$  are the observational zenith and azimuth angles, respectively.  $L_S$  is the radiance leaving the source in the azimuth of the observer. We assume azimuthal symmetry of the source emissions.

Analogously to the solution concept we have implemented in [Kocifaj and Bará \(2019\)](#), we use the Henyey-Greenstein (HG) function to describe the shape of the total scattering phase function  $P(g, \theta)$ . The HG function is also known to provide reasonably accurate predictions for aerosol ensembles, provided that the asymmetry parameter  $g_a$  used is accurate ([Kahnert et al. 2005](#)). Therefore we substitute  $P_a(g_a, \theta)$  for its HG-equivalent. The Rayleigh scattering phase function  $P_R(\theta)$  can be expressed analytically in the form of  $\frac{3}{4}(1 + \cos^2 \theta)$ . The functions  $M(z)$  and  $M_S$  in Eq. 2 are the optical air mass in directions of  $z$  and the light source, respectively.

It is reasonable to expect that in a non-turbid, but still multiple-scattering atmosphere,  $P(g, \theta)$  still displays some degree of anisotropy which can be modelled by  $P_0(g_0, \theta)$  with  $g_0 > 0$ . We assume that in a turbid atmosphere  $P(g, \theta)$  be a non-trivial superposition of the basis functions  $P_0(g_0, \theta)$  and  $P_a(g_a, \theta)$ .

## 3 INPUTS TO THE MODEL

An exceptional simplification of otherwise vast numerical modelling of NSB distributions arises from the separation of variables concept, which is a peculiar property of the model developed. The key element which makes the model really strong is the proper adjustment of the input parameters  $t$  and  $g$ .

### The parameter $t$

Due to its nature the product of  $t$  and  $M_S$  determines the optical transmission coefficient ( $e^{M_S t}$ ) of the atmospheric volume between the source of light and the observer. Assuming the beam of light traverses the atmosphere horizontally, the intensity decays proportionally to  $e^{-T}$ , where  $T = (k_a + k_R)D$ ;  $D$  being the separation distance between source of light and observer. By satisfying an identity criterion for both exponential functions, we obtain

$$t = \left( \frac{\tau_a}{H_a} + \frac{\tau_R}{H_R} \right) \frac{D}{M_S}, \quad (3)$$

where  $\tau_a$  and  $H_a$  are the aerosol optical thickness of a vertical atmospheric column and the aerosol scale height, respectively. The respective parameters for air molecules are  $\tau_R$  and  $H_R$ . Eq. 3 is valid for an exponential atmosphere with vertical stratification of aerosol concentration being proportional to  $k_a e^{-h/H_a}$ ;  $h$  is the altitude above the ground. The vertical distribution of air molecules is modelled analogously, so  $k_R e^{-h/H_R}$ .

### The parameter $g$

No suitable analytical expression for parameter  $g$  exists yet. We have retrieved  $g$  by matching the modelled NSB distributions to the ones obtained from highly accurate multiple scattering computations ([Kocifaj 2018](#)). The latter allows for modelling the higher-scattering diffuse radiance of the night sky at arbitrary altitude, horizontal separation, and spectral band. It is highly important to determine  $g$  in a narrow spectral band, first because  $g$  is wavelength-dependent, and also because the exact solution to the governing equations (and underlying Maxwell equations)

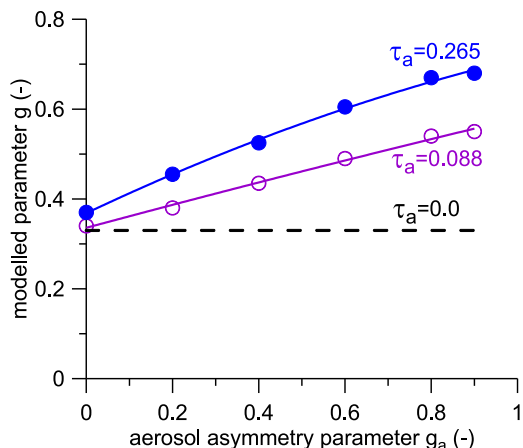


**Figure 1.** The parameter  $g$  as a function of aerosol asymmetry parameter  $g_a$  for three discrete values of aerosol optical depths ( $\tau_a$ ).

normally requires the concept of perfectly monochromatic radiation.

Here we show the solution for wavelength  $\lambda=550$  nm, located in the middle of the visible spectrum. Considering a relatively smooth variation of the atmospheric scattering properties, the results we obtain are also representative for adjacent wavelengths, roughly located in a spectral band of width  $\pm 20$ -30 nm. An advantageous feature of such computations is that the above spectral band overlaps with the dominant emissions from LPS, HPS, MH, or MV lights, and also with the phosphor re-emission peak of pc-LED spectra.

The optimum value of  $g$  is determined by minimizing the differences between the radiance distribution modelled from Eq. 2 and the one computed as a sum of five scattering orders (Kocifaj 2018). The parameter  $g$  is shown in Fig. 1 as a function of  $g_a$  for three discrete aerosol optical depths. The results are in conformity with our premise that  $P(g, \theta)$  asymptotically approaches that of  $P_0(g_0, \theta)$  with  $g_0 \approx 0.33 > 0$ ; which excludes isotropic scattering patterns even if the aerosol optical thickness is nearly zero. The approximate formula we have found for  $g$  is as follows

$$g = c_0 + c_1 g_a + c_2 g_a^2, \quad (4)$$

with

$$\begin{aligned} c_0 &= 0.33 + 0.15\tau_a \\ c_1 &= 0.9\tau_a^{0.51} \\ c_2 &= 1.3\tau_a^{1.85}. \end{aligned} \quad (5)$$

#### Input data

Ground-based monitoring networks such as the Aerosol Robotic Network (AERONET) normally provide the best opportunities to characterize aerosols in the lower atmosphere. Unfortunately, ground stations are sparsely distributed, making it difficult a global aerosol mapping (Wei et al. 2020). However, aerosol satellite products with wide-scale coverage are a useful source of information on global distribution of  $\tau_a$  and  $g_a$  (Shikwambana and Sivakumar 2018). Satellites orbiting the Earth collect real-time data, thus updating aerosol parameters dynamically by region and season (Remer et al. 2005).

Consistent records of the Earth’s aerosol system are available through the Moderate Resolution Imaging Spectroradiometer (MODIS) on NASA’s Terra satellite (MODIS 2022; TERRA 2022). Missing aerosol data can be interpolated or inferred based on the aerosol types persistently prevalent in the region/season or based on the information on dominant aerosol emission sources in a local or regional context. This is possible since a global aerosol climatology project has shown that the aerosol optical properties at 550 nm depend markedly on aerosol types, specifically on whether fine-mode or coarse-mode particles dominate the regional emissions. The project has also analysed aerosols of anthropogenic origin, dust, sulfates, nitrates, sea-salts and organic-matter (Kinne et al. 2013; Kinne 2019).

#### Artificial light sources

The radiance of the light sources surrounding the observer is another key input for calculating the artificial all sky brightness. Monochrome and RGB imagery of artificial light emissions with nearly worldwide coverage is presently provided by several on-orbit radiometers (Elvidge et al. 2017, 2021; Levin et al. 2020; ?; Zheng et al. 2018) as well as by the Crew Earth Observation program of the International Space Station (Sánchez de Miguel et al. 2019, 2021; Stefanov et al. 2017). These inputs are expected to be enough for computing world hemispheric sky brightness maps with a level of accuracy comparable to that already attained by their zenith counterparts (Falchi et al. 2016). Earth observation at nighttime is a thriving field and it can be anticipated that observing platforms with enhanced spectral and angular sensing capabilities will be planned and developed in the next years.

The final calculation of the hemispheric radiance, for any given observing site, is made by adding up the individual hemispheric contributions of each light source. Within the range of validity of the model here presented, the contributions of sources located at equal distances from the observer but different azimuths are just rotated versions of the same basic pattern, weighted by the radiance emitted by each source in the direction to the observer. The computational burden can be further alleviated by pre-calculating the model parameters for a dense set of different distances, atmospheric conditions, angular and spectral source emission patterns and observation photometric bands.

## 4 MODEL CORROBORATION

We have used the functionality of the multiple scattering code MSOS1 Kocifaj (2018) to accurately model the night sky radiance distributions for the wavelengths of 550 nm and 450 nm, two aerosol scale heights ( $H_a=1.5$  km and 2.2 km) and a set of discrete aerosol asymmetry parameters ( $g_a$ ) ranging from 0 to 0.9. Single scattering albedo of aerosols  $\omega_a$  is typically as large as 0.95 which allows for substitution of volume scattering coefficient  $\omega_a k_a$  for volume extinction coefficient  $k_a$  in our numerical runs and thus reduce the degrees of freedom. The exact computations are performed up to fifth scattering order to guarantee that multiple scattering radiances are accurate to within a few tenths of percent for all grid points on the modelling domain.

We first validate the model for an aerosol-free atmo-

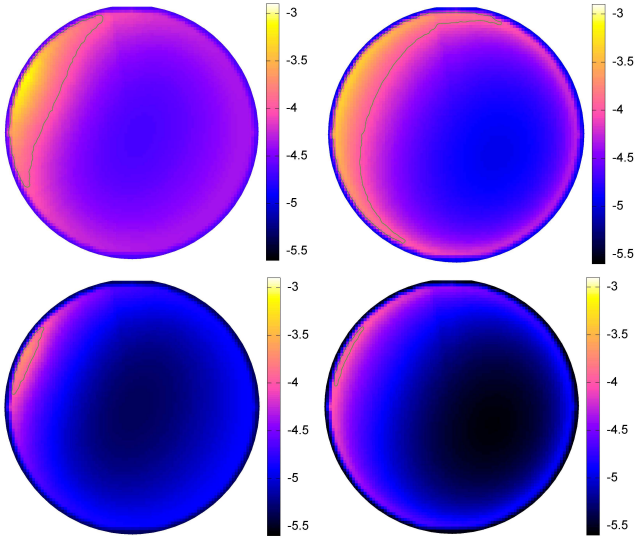


**Figure 2.** All plots are false color images of the night sky radiance distributions at 450 nm for a light source seen at the azimuth angle of  $294^\circ$ . For each figure the azimuth is measured in a clockwise direction (with north at the top). The zenith and horizon ( $z = 85^\circ$ ) are in the center and at the edge of each plot, respectively. Left column shows results of exact computations using a multiple scattering code (Kocifaj 2018), right column is for the model (Eq. 2). Top panels are for the horizontal distance of  $D=7\text{km}$ ; bottom panels are for  $D=15\text{km}$ . Radiance data in arbitrary units are plotted on a logarithmic scale. The aerosol optical depth is  $\tau_a=0$ , while the remaining input data are in described in the main text.

sphere ( $\tau_a = 0$ ). In this case the results should be independent of any aerosol properties. This not only makes the model validation in limit conditions possible, but also provides an ideal starting point for increasingly detailed study. Fig. 2 documents that the modelled radiance distribution at 450 nm (right column) matches the exact computations (left column). The radiance data are shown on the same logarithmic scale to allow for reasonable comparison. The best fit parameter  $g_0 = 0.36$  for the wavelength of 450 nm is a bit higher than that for 550 nm (see Fig. 1). However, this finding is fully consistent with what has been indicated earlier – specifically that  $g$  (and  $g_0$  as well) should exhibit spectral features. The mean discrepancy of modelled and computed radiance averaged over all sky elements is 20%.

The same type analysis is being applied to  $\tau_a = 0.23$ , which corresponds to a moderately polluted atmosphere. AODs around 0.2 not only belong to the most abundant class of aerosol optical depths (see e.g. Markowicz et al. (2021)), but are also representative for marine and continental aerosol systems (Welton et al. 2002). Fig. 3 demonstrates the model’s ability to produce reasonable predictions for a turbid atmosphere, with even a highly anisotropic scattering function  $P(\theta)$  and radiance amplitudes varying over several orders of magnitude. It is well documented that the aerosol particles make  $P(\theta)$  strongly forward-lobed, which along with increased extinction at the blue edge of the visible spectrum results in transitioning from slight to steep NSB gradation. To demonstrate the effect of increased forward scattering from large particles we conducted numerical experiment on  $P_a(g_a, \theta)$  with  $g_a=0.85$ , which is a typi-

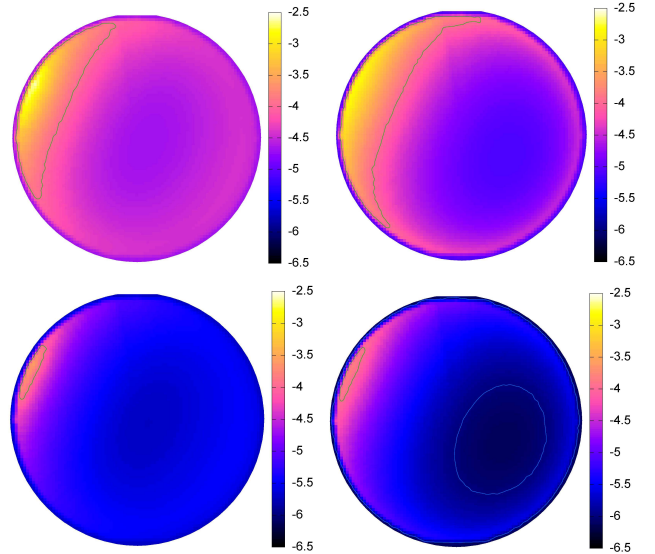


**Figure 3.** The same as in Fig. 2, but for  $\tau_a=0.23$  and aerosol asymmetry parameter  $g_a=0.85$ .

cal value for water aerosols (Peng and Li 2016; Graaf et al. 2005). Large particles may have tendency to concentrate in the lower atmosphere, thus we chose  $H_a$  as low as 1.5 km. The mean discrepancy between modelled and accurately computed radiance distributions is 20-25%. The solution obtained for heavily polluted atmosphere ( $\tau_a=0.57$ , not shown here) keeps the same error margin.

Systematic computations for green light (550 nm) using multiple scattering tool include situations with  $\tau_a=(0.0, 0.088, 0.265)$ ,  $g_a=(0, 0.2, 0.4, 0.6, 0.8, 0.9)$ , and  $D=(1.3, 2.9, 6.7, 15.4, 35.3, 81.3)$ . The overall deviation of modelled from accurately computed NSB distributions ranges from 15% to 25%. The proposed model was successful to simulate low and high aerosol contents, even the aerosol systems with  $\tau_a$  exceeding  $\tau_R$  by a factor of 2-3. The model works well for all aerosol asymmetry parameters studied, as documented in Fig. 4 for  $g_a=0.4$  and 0.9. This makes us confident that the model can significantly compensate the effort that otherwise would be needed for systematic long-term sky surveys worldwide.

## 5 DISCUSSION

The analytical expression in (Eq. 2), with the appropriate values of  $g$  and  $t$  for each wavelength, atmospheric conditions, and distance to the observer, provides an easy way of computing the radiance distribution in all sky directions above the observer. The angular resolution can be set with no difficulty at the level required for each application. The overall all-sky map produced by the artificial sources located in the territory surrounding the observer is built up by adding the contributions of each individual source. The contributions of sources located at a constant distance and different azimuths are just rotated versions of the same basic pattern. Note also that due to the linear nature of the atmospheric light propagation processes at the radiance levels typical of outdoor lighting systems, wide band all-sky radiance distributions in function of the distance to the observer



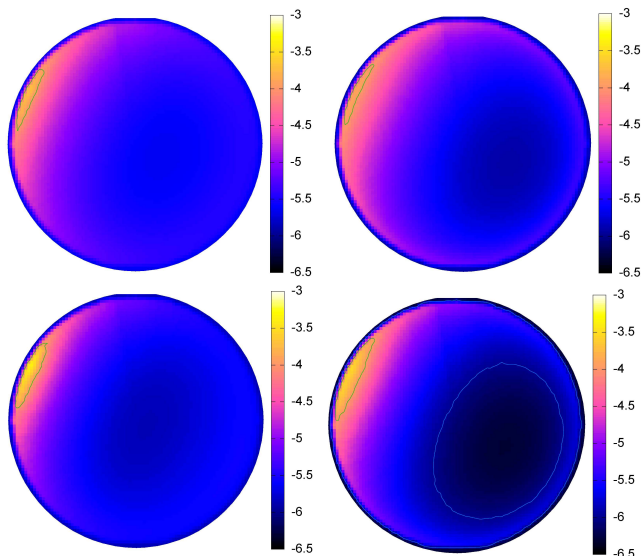


**Figure 4.** The same as in Fig. 2, but for wavelength of 550 nm,  $\tau_a=0.265$ ,  $H_a=2.2$  km, and  $D=15$ km. Top panels are for aerosol asymmetry parameter  $g_a=0.4$ , while the bottom panels are for  $g_a=0.9$ .

can be computed in advance for each class of source (defined as having a given spectral and angular emission pattern) saving additional computation time.

The examples in the sections above are intended to provide basic insights about the performance of this approach. They correspond some simplified situations (e.g. the effects of obstacles and terrain elevation have not been included), and could be applied to more complex environments without any fundamental difficulty. Our approach is basically independent of the particular models and routines chosen by the interested researcher for computing the artificial radiance of the sky: it is designed to provide an efficient representation of the final results, and could be applied to propagation models that would provide the optimum values of  $g$  and  $t$  in function of different sets of basic atmospheric and source emission parameters.

## 6 CONCLUSIONS

We present in this work an analytical formula for the hemispherical spectral radiance produced by an artificial light source, that allows to streamline the process of computing the all-sky artificial brightness map for observers located at any place in the world. This expression depends on two basic parameters, whose optimal values are contingent the on atmospheric conditions, source emission patterns, and distance to the observer, and can be determined by approximate analytic expressions or adequate look-up tables. This approach provides a substantial reduction in the number of free parameters required to describe the all-sky radiance produced by a ground-level elementary light source.

## ACKNOWLEDGEMENTS

This work was supported by the Slovak Research and Development Agency under contract No: APVV-18-0014. Computational work was supported by the Slovak National Grant Agency VEGA (grant No. 2/0010/20).

## DATA AVAILABILITY STATEMENT

The numerical results for the all-sky radiance distributions were computed using the model developed here and that available in (Kocifaj 2018). We did not use any new data.

## REFERENCES

- Bará S. et al., 2015a, *Appl. Opt.* 54, 4120  
Bará S. et al., 2015b, *J. Opt.* 17, 105607  
Cinzano P., Falchi F., Elvidge, C., 2001, *MNRAS* 328, 689  
Elvidge C. D. et al., 2017, *Int. J. Remote Sens.* 38, 5860  
Elvidge C. D. et al., 2021, *Remote Sens.* 13, 922  
Falchi F. et al., 2016, *Sci. Adv.* 2, e1600377  
Fokou A. et al., 2021, *JQSRT* 270, 107707  
de Graaf M. et al., 2005, *JGR* 110, D01201  
Kahnert M., Nousiainen T., Veihelmann B., 2005, *JGR* 110, D18S13  
Katkovsky L. V. et al., 2018, *Rem. Sens.* 10, 1698  
Kinne S. et al., 2013, *J. Adv. Model. Earth Syst.* 5, 704  
Kinne S., 2019, *Tellus B* 71, 1623639  
Kocifaj M., 2018, *JQSRT* 206, 260  
Kocifaj M., Bará S., 2019, *MNRAS* 490, 1953  
Levin N. et al., 2020, *Remote Sens. Environ.* 237, 111443  
Li X. et al., 2022, *Remote Sens. Environ.* 271, 112920  
Markowicz K. M., Zawadzka-Manko O., Posyniak M., 2021, A large reduction of direct aerosol cooling over Poland in the last decades, *Int. J. Climatol.* (in press)  
Mobley C. D., 2015, *Appl. Opt.* 54, 4828  
<https://modis.gsfc.nasa.gov/> (Last accessed, February 2, 2022)  
Peng P., Li C., 2016, *Appl. Opt.* 55, 3903  
Remer L. A., et al., 2005, *J. Atmos. Sci.* 62, 947  
Sánchez de Miguel A., et al., 2019, *Remote Sens. Environ.* 224, 92  
Sánchez de Miguel A., et al., 2021, *Remote Sens. Environ.* 264, 112611  
Shikwambana L., Sivakumar V., 2018, *J. Atmos. Sol. Terr. Phys.* 173, 150  
Stefanov W. L. et al., 2017, in *Handbook of Satellite Applications*, Springer International Publishing Switzerland.  
<https://terra.nasa.gov/> (Last accessed, February 2, 2022)  
Wei J. et al., 2020, *Atmosph. Environ.* 240, 117768  
Welton E. J. et al., 2002, *JGR* 107, 8019  
Zheng Q. et al., 2018, *Remote Sens. Environ.* 215, 300

This paper has been typeset from a  $\text{\TeX}$ / $\text{\LaTeX}$  file prepared by the author.